Available online at www.sciencedirect.com
ScienceDirect
Trans. Nonferrous Met. Soc. China 34(2024) 755−768
Transactions of Nonferrous Metals Society of China
www.tnmsc.cn

Influence of aging treatment on corrosion behavior of extruded 2195 Al−Li alloy

Hui LI[1,2], Zhi-wen WANG[3], Rong FU[1,2], Yuan-chun HUANG[1,2,3]

1. School of Mechanical and Electrical Engineering, Central South University, Changsha 410083, China;
2. State Key Laboratory of High-Performance Complex Manufacturing, Central South University, Changsha 410083, China;
3. Light Alloy Research Institute, Central South University, Changsha 410083, China

Received 25 August 2022; accepted 17 April 2023

Abstract: The 2195 Al-Li alloy was processed by under-aging (UA), peak-aging (PA), double-aging (DA) and retrogression re-aging (RRA) treatments, and the microstructure, intergranular corrosion (IGC), exfoliation corrosion (EXCO) and stress corrosion cracking (SCC) behaviors were observed and discussed. The results show that the sequence of IGC and EXCO resistance is: RRA > UA > DA > PA. The low corrosion resistance of PA and UA is mainly caused by the continuous precipitation of T_1 phases at grain boundaries to form continuous corrosion channels, while the interruption of corrosion channels caused by coarse and discontinuous T_1 phases and wider precipitate free zone is the reason for the best corrosion resistance of RRA. The RRA alloy exhibits the best SCC resistance, and the order of SCC resistance is: RRA > DA > UA > PA. The discontinuous precipitation of intergranular T_1 phases promotes the propagation of corrosion cracks across grain boundaries, thereby improving the SCC resistance.
Key words: aging; microstructure evolution; corrosion behavior; corrosion mechanism

1 Introduction

2195 Al−Li alloy is a third-generation alloy that finds widespread use in the aerospace industry, such as cryogenic fuel tanks of launch vehicles, wall plates, long trusses, and floor beams of large aircraft, owing to its superior mechanical properties [1−4]. However, when exposed to moist air or saline environments, the grain boundary precipitates of alloy are prone to forming corrosion microcells with the surrounding matrix, rendering it susceptible to intergranular corrosion (IGC) and exfoliation corrosion (EXCO) [5]. The situation is further compounded by the possibility of stress corrosion cracking (SCC) if the alloy is subjected to tensile and compressive stresses during its operation. Therefore, there is an urgent need to enhance the corrosion resistance of 2195 Al−Li alloy to ensure its safe and effective application in the aerospace industry. Relevant studies [6−8] have shown that the corrosion behavior of aluminum alloy is mainly controlled by the micro-chemical composition at the grain boundary, and has little relationship with the size and morphology of precipitates in the matrix. It is generally believed that the distribution of precipitates at grain boundaries and the width of the precipitation free zone (PFZ) play a critical role in corrosion susceptibility, while the uniform precipitates cannot be ignored [9−11].

At present, the research according to the influence of aging treatment on the corrosion performance of 2195 Al−Li alloy mainly focuses on

Corresponding author: Yuan-chun HUANG, Tel: +86-13507315123, E-mail: ychuang@csu.edu.cn
DOI: 10.1016/S1003-6326(23)66432-5

single-stage aging and artificial aging after pre-deformation, but few studies on multi-stage aging and retrogression re-aging (RRA). HOLROYD et al [12] analyzed the mechanisms under aging (UA), peak aging (PA) and over aging (OA) on the corrosion susceptibility of Al−Li alloys, and the results showed that the corrosion susceptibility of IGC gradually increases as copper content of alloy and aging time increase, while the EXCO resistance of PA is inferior to that of UA and OA. According to SCC, different Al−Li alloys exhibit different corrosion susceptibilities, e.g., crack initiation and propagation susceptibility of AA 8090 decrease with the extension of aging time, while AA 2090 displays the same results for SCC resistance as for EXCO. LIN et al [13] used T8 duplex aging treatment to obtain densely distributed T_1 phases inside grains and discontinuously distributed second phases at the grain boundaries, which greatly reduced the difference of corrosion potential between matrix and grain boundaries, resulting in declining IGC susceptibility. ROMIOS et al [14] inferred that compared to the T861 state, the strength of 2099 Al−Li alloy during multistep aging slightly decreased, while the anisotropy is reduced. RRA treatment was originally proposed to improve the stress corrosion resistance of 7075 aluminum alloy, which combines the advantages of T6 and T73 to improve the strength of the alloy while also improving the resistance of alloy to EXCO and SCC, and has been widely used in Al−Zn−Mg and Al−Zn−Mg−Cu alloys [15−19]. However, for Al−Li alloys, the optimum temperature and time that can be regulated during the retrogression treatment are relatively small, limiting the application of the process to large-size profiles, therefore, few researchers have paid attention to RRA treatment of Al−Li alloys. GHOSH et al [20,21] studied the microstructure evolution of main precipitates in 8090 and 1441 Al−Li−Cu−Mg−Zr alloys during RRA, it demonstrated that the strength obtained by RRA treatment was similar to that of the conventional PA treatment, but it contributed to the growth of δ, S' and T_1 phases, meanwhile the reduction of dislocation density and the generation of more dislocation loops and helices simultaneously. WARD et al [22] found that the ultimate and yield strength decreased with increasing retrogression time and temperature, and the variation in elongation was vague.

Until now, few investigations on the couple effects of single-stage and multi-stage aging on the behavior of IGC, EXCO and SCC of Al−Li alloys have been discussed, particularly in the corrosion mechanism of large-size extruded profiles of 2195 Al−Li alloy. The aim of this work is to investigate the influence of different artificial aging treatments on the size, distribution and elemental composition of precipitates of grain interior and grain boundary of 2195 Al−Li alloy, and illustrate the influence mechanism of various microstructures on the corrosion resistance. Finally, an optimized aging scheme was proposed to balance mechanical properties and corrosion resistance of extruded 2195 Al−Li alloy profiles.

2 Experimental

2.1 Material and heat treatments

The experimental material Al−3.98Cu−0.99Li−0.32Mg−0.32Ag−0.12Zr−0.08Fe−0.04Si (wt.%) was hot extruded and provided by the Southwest Aluminum (Group) Corporation Ltd., China. The profile was extruded under the working conditions that the billet temperature is 420 °C, the die temperature is 410 °C, and the extrusion speed is 0.2 mm/s. The samples were uniformly prepared with a solid solution at 520 °C for 1 h with rapid water cooling to produce supersaturated solid solutions. Subsequently, block samples of various sizes and standard tensile samples were cut from the profiles. Following that, the solid solution samples were subjected to various artificial aging processes, including under aging (UA), peak aging (PA), double aging (DA), and retrogression re-aging (RRA), as shown in Table 1. The dimensions of the profiles, the sampling locations of the block samples and the dimensions of the slow strain rate tensile samples are shown in Fig. 1.

Table 1 Aging treatments for 2195 Al−Li alloy

Schedule	Description
UA	170 °C, 6 h
PA	170 °C, 36 h
DA	(120 °C, 8 h) + (170 °C, 18 h)
RRA	(170 °C, 18 h) + (220 °C, 40 min) + (170 °C, 36 h)

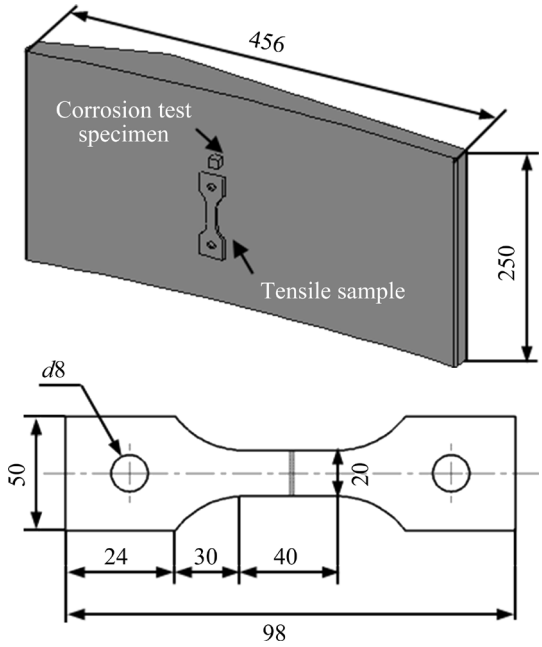

Fig. 1 Sampling locations and dimensions of tensile samples (Unit: mm)

2.2 Microstructure observation

The microstructure and IGC depth of the samples were observed by optical microscopy (OM). The transmission electron microscopy (TEM, FEI Tecnai G^2 F20) was used to observe the types and morphologies of the precipitates forming at the boundary and inside of grain of the alloy under different aging regimes. The samples for TEM testing were manually ground to a thickness of 80 μm, punched into 3 mm-diameter discs, and then twin-jet electropolished in 30% HNO_3 + 70% CH_3OH solution at −25 °C, and the voltage was controlled at 15 V. The microstructure and tensile fracture morphology were observed using a scanning electron microscope (SEM, JSM−7800F), and the chemical composition of precipitates was examined using an energy dispersive spectrometer (EDS, Xmax−80).

2.3 Intergranular corrosion tests

The addition to the implementation IGC tests was in accordance with GB/T 7998−2005 standard. The corrosion samples were intended to be 5 mm × 10 mm × 10 mm, and after pretreatment with 10% NaOH solution and 30% HNO_3 solution, samples were put into the corrosive solution (each liter of solution contains 57 g NaCl + 10 mL H_2O_2) for 6 h, and the temperature of the solution was controlled at (35±2) °C. The corroded samples were then washed and dried with water and cut off by 5 mm along the vertical extrusion direction. Finally, the corrosion samples were prepared according to the metallographic sample preparation method, and the intergranular corrosion depth was observed under the OM.

2.4 Exfoliation corrosion tests

The EXCO tests were carried out according to GB/T 22639−2008. The corrosion samples were cut along the extrusion direction to a size of 10 mm × 10 mm × 30 mm, the non-denuded surface was sealed with denture base resin, only exposing the denuded surface. Then, after polishing the samples until the surface was bright and free of scratches, the EXCO tests were carried out. The corrosive solution adopts the mixed solution of 4 mol/L NaCl + 0.5 mol/L KNO_3 + 0.1 mol/L HNO_3, and the temperature was controlled at (25±2) °C. After being immersed in the corrosive solution for 96 h, the samples were removed, washed, and dried with distilled water. The corrosion morphologies of the samples' surfaces and cross-sections were then observed using OM.

2.5 Stress corrosion cracking tests

According to GB/T 15970.7−2000, the slow strain rate tensile test was used to conduct the SCC tests. The dimensions of the transversely collected samples utilized for the SCC tests are presented in Fig. 1, and the dimensions are performed with reference to GB/T 228. The tensile tests were conducted at (35±1) °C with a strain rate of 1×10^{-6} s^{-1} in air and 3.5% NaCl corrosive solution, respectively. SEM observations of the 2195 alloy fracture morphologies following the fracture were obtained.

3 Results

3.1 Microstructure after solid solution

The microstructure of the extruded 2195 Al−Li alloy after solid solution treatment is shown in Fig. 2. It can be seen from the OM in Fig. 2(a) that the grains are flattened and elongated along the extrusion direction in the shape of slender fibers. And simultaneously, fine equiaxed new grains can be observed between some large grains, indicating that partial dynamic recrystallization occurred

during the extrusion process. As can be seen in Fig. 2(b), after solid solution treatment, the vast majority of the second phase particles re-dissolved back into the matrix, leaving only a small number of larger insoluble second phase particles. The chemical composition analysis of part of the second phase particles using EDS reveals that the intermittently distributed irregular bulk phase in the matrix is Al−Cu−Fe phase and the fine spherical phase with dispersed distribution is Al−Cu−Zr phase.

3.2 Microstructure under different artificial aging treatments

The STEM micrographs and corresponding selected area diffraction patterns (SADPs) taken along $\langle 011 \rangle_{Al}$ zone axis of 2195 Al−Li alloy at different aging treatments are shown in Fig. 3. As can be seen in Figs. 3(a−d), spherical, discoidal and needle-like second phases of different morphologies and sizes all precipitated from the supersaturated solid solution during aging, with the smaller spherical precipitated phase being the δ'/β' (Al_3Li,Zr) phase and the needle-like second phase being the T_1 (Al_2CuLi) phase. Comparing the SADPs of Figs. 3(e−h) with the standard diffraction patterns [23], it is possible to determine the type of precipitates at different aging stages.

From Figs. 3(a,b), it can be seen that the number and size of precipitates in the alloy are larger in the PA state compared with the UA state. In the UA state, needle-like T_1 phases with larger spacing and lengths of 80−120 nm are precipitated in the matrix. Meanwhile, spherical δ' (Al_3Li) phases

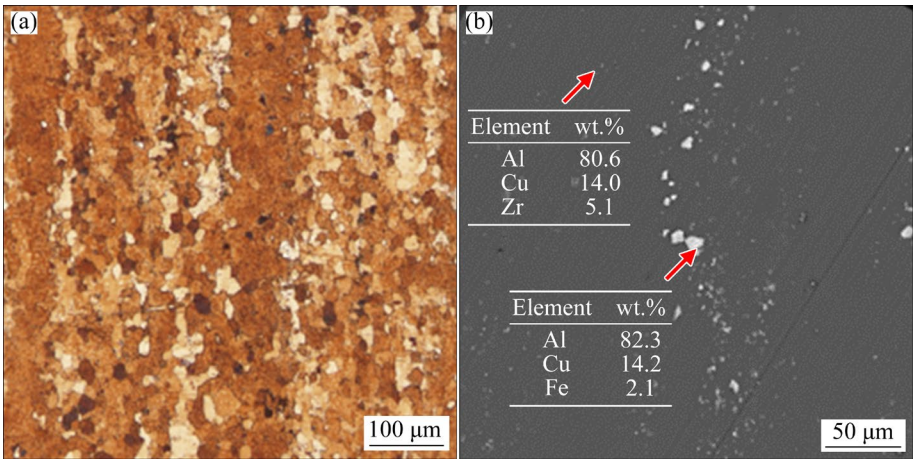

Fig. 2 OM (a) and SEM (b) morphology of extruded 2195 Al−Li alloy after solid solution treatment

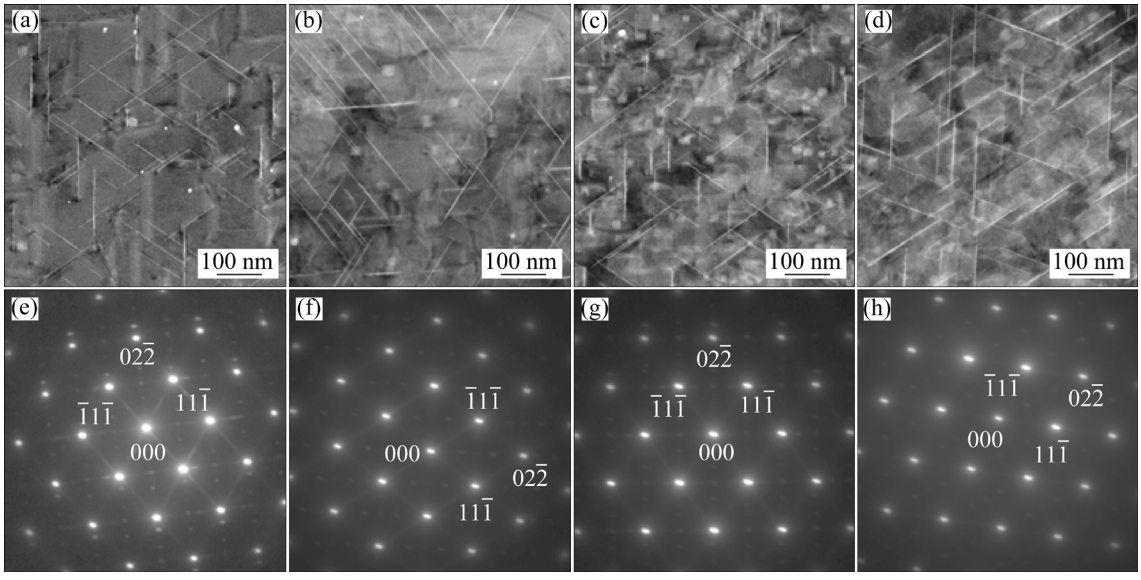

Fig. 3 STEM micrographs (a−d) and corresponding selected area diffraction patterns (SADPs) (e−h) taken along $\langle 011 \rangle_{Al}$ zone axis of 2195 Al−Li alloy in different aging states: (a, e) UA; (b, f) PA; (c, g) DA; (d, h) RRA

with diameters of 5−10 nm are uniformly distributed in the matrix, and δ'/β' composite phase particles with diameters of 20−30 nm are also observed. Analysis of the corresponding SADPs shows that the diffraction streaks in the $\langle 002\rangle_{Al}$ direction are relatively bright, indicating that a large amount of θ' phase is also precipitated in the matrix during UA. According to the SADP, it can be seen that the diffraction spot intensity of the T_1 phase increases significantly, while the diffraction spot corresponding to the δ' phase becomes weaker and the diffraction spot of the θ' phase almost disappears, which further confirms that the extension of the aging time will cause the reduction of the δ' and θ' phases and correspondingly promote the precipitation and growth of the T_1 phase [24]. It can be seen from Fig. 3(c) that the density of precipitated phases in the matrix is higher and more uniformly distributed after DA treatment compared to other aging processes. The largest number of spherical δ'/β' phases and rod-shaped θ' phases with sizes ranging from 30 to 50 nm are precipitated in the matrix, and the size of the precipitated T_1 phase is relatively small compared to that of the PA. The analysis of Fig. 3(d) shows that the T_1 phases with relatively large length and width are mainly precipitated in the matrix after RRA, the spherical δ'/β' phase basically disappears, and the corresponding diffraction spots also prove that the main precipitated phase in the alloy is the T_1 phase (Fig. 3(h)).

The STEM micrographs of grain boundary phases in samples treated with different aging processes are shown in Fig. 4. It can be seen that the precipitated phases at the grain boundaries are continuously distributed in both UA (Figs. 4(a, b)) and PA states (Figs. 4(c, d)), and the size of the precipitated phases in the PA state is significantly larger than that in UA state, but the width of the PFZ is basically unchanged, which is around 100 nm. In the DA state (Figs. 4(e, f)), the overall distribution of the precipitated phases at the grain boundaries is continuous, but in some areas, they appear as discontinuous particles of different sizes, and the width of the PFZ band decreases to 92 nm. In the RRA state (Figs. 4(g, h)), the size of the precipitates at the grain boundaries increased significantly and distributed intermittently, reaching a PFZ width of 125 nm.

EDS surface scanning was used to analyze the chemical composition of precipitates in the RRA state in order to further identify the different types

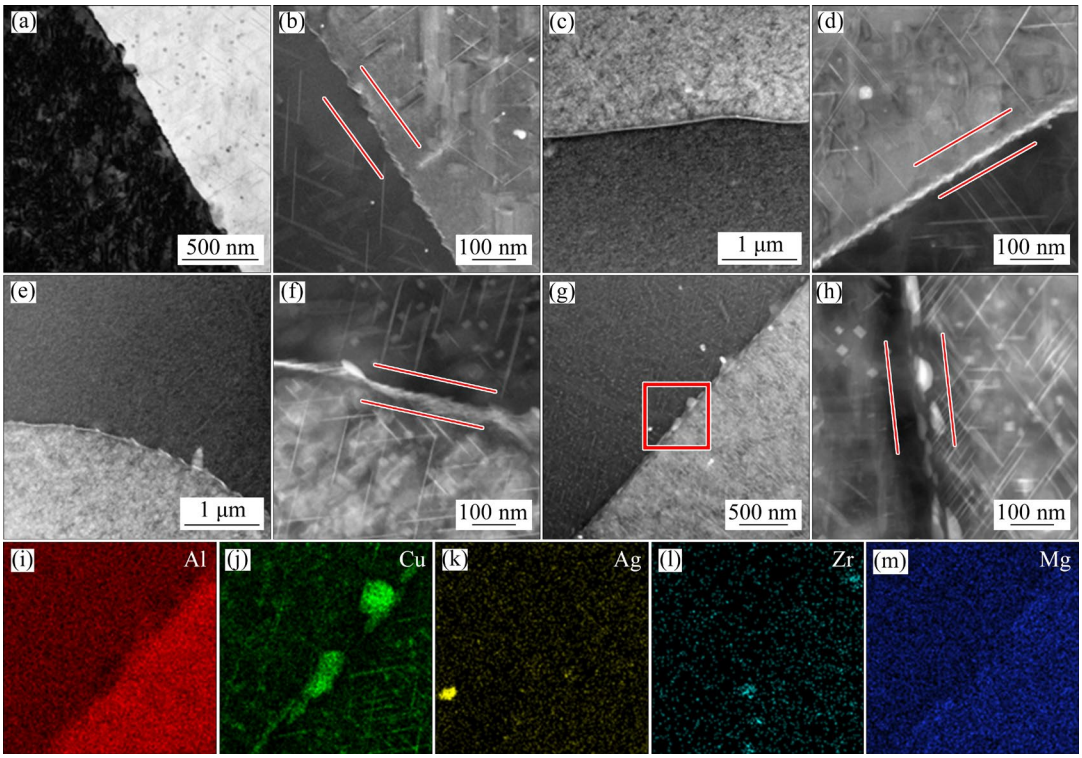

Fig. 4 STEM micrographs (a−h) of grain boundary phases in samples treated by different aging processes and corresponding element distributions (i−m): (a, b) UA; (c, d) PA; (e, f) DA; (g, h) RRA; (i−m) Element distribution of zone in (g)

of grain boundary precipitates, and the results are depicted in Figs. 4(i−m). The intermittently scattered precipitates near the grain boundary are largely enriched in Cu elements, as seen in Fig. 4(j), with a little amount of Zr elements also appear. These substances can facilitate the nucleation and precipitation of T_1 phase [25,26]. In addition, more Zr elements are diffusely distributed in the crystal, forming the β' phase and acting as the heterogeneous nucleation core of the δ' phase [27].

The Li element is too light, and its associated energy is too low for EDS analysis, making it impossible to detect the type of grain boundary precipitates. Therefore, a high-resolution examination using the HRTEM technique was carried out to identify the massive and granular grain boundary precipitates shown in Figs. 4(g) and (h). The results of this examination are displayed in Fig. 5. The SADP of the precipitates was obtained through the corresponding Fast Fourier Transform (FFT) of Fig. 5(a). By comparing it with the standard SADP, it was determined that the intermittently distributed massive and granular precipitates at the grain boundaries are T_1 phases, which is consistent with the results of HUANG et al [28].

3.3 IGC behavior

The IGC morphologies of the 2195 Al−Li alloy in different aging states are depicted in Fig. 6, highlighting substantial differences in corrosion morphology following immersion in the IGC solution in different aging states. Figure 6(a) exhibits an obvious non-uniform distribution of corrosion pits with a depth of 47.2 μm on the surface of alloy, indicating that corrosion primarily occurs in localized regions and relies mainly on pitting corrosion while the alloy is in the UA state. The corrosion profile of the alloy after PA treatment demonstrates that the corrosion pits spread into the grain, and their diameter significantly increases compared to the UA state, with a corrosion depth of 62.1 μm, but with no significant IGC characteristics. After DA treatment, the corrosion surface of the alloy is irregular, and the corrosion pits are continuously distributed, with a depth of 48.3 μm, indicating that DA can reduce the corrosion susceptibility of the alloy to some extent compared with PA. After RRA treatment, the corrosion pits are discontinuous at the corrosion interface, and the intergranular corrosion phenomenon and corrosion degree of the alloy are lower than those in other aging states, with a maximum corrosion depth of 46.5 μm, close to that of UA. Moreover, some coarse second-phase particles at the bottom of the corrosion pits may be the primary cause of pitting corrosion. This result indicates that the 2195 Al−Li alloy after RRA treatment has a high resistance to IGC.

3.4 EXCO behavior

Figure 7 depicts the exfoliation corrosion morphologies of the 2195 Al−Li alloy in different aging states after 96 h immersion in EXCO solution. The surface of the alloy with different aging treatments displays different degrees of delamination and peeling, and some corrosion products are detached. Further analysis reveals that the surface of the alloy after UA treatment experiences a large-scale explosion and powdering. After PA treatment, the phenomenon of explosion and powdering on the alloy surface is very severe, with a large area of delamination and peeling. Moreover, some inner layers have peeled off, with more corrosion products, and larger and deeper pits

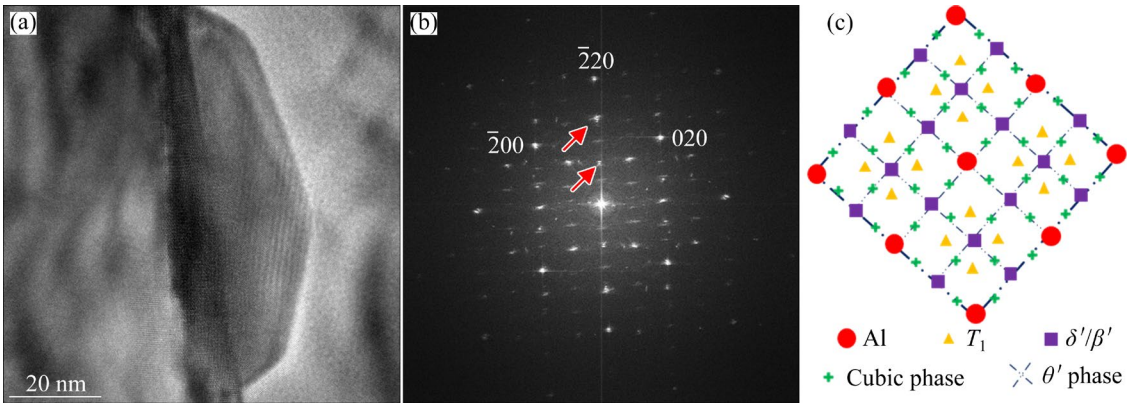

Fig. 5 HRTEM image (a) and corresponding FFT patterns (b, c) of grain boundary phase in alloy at RRA state

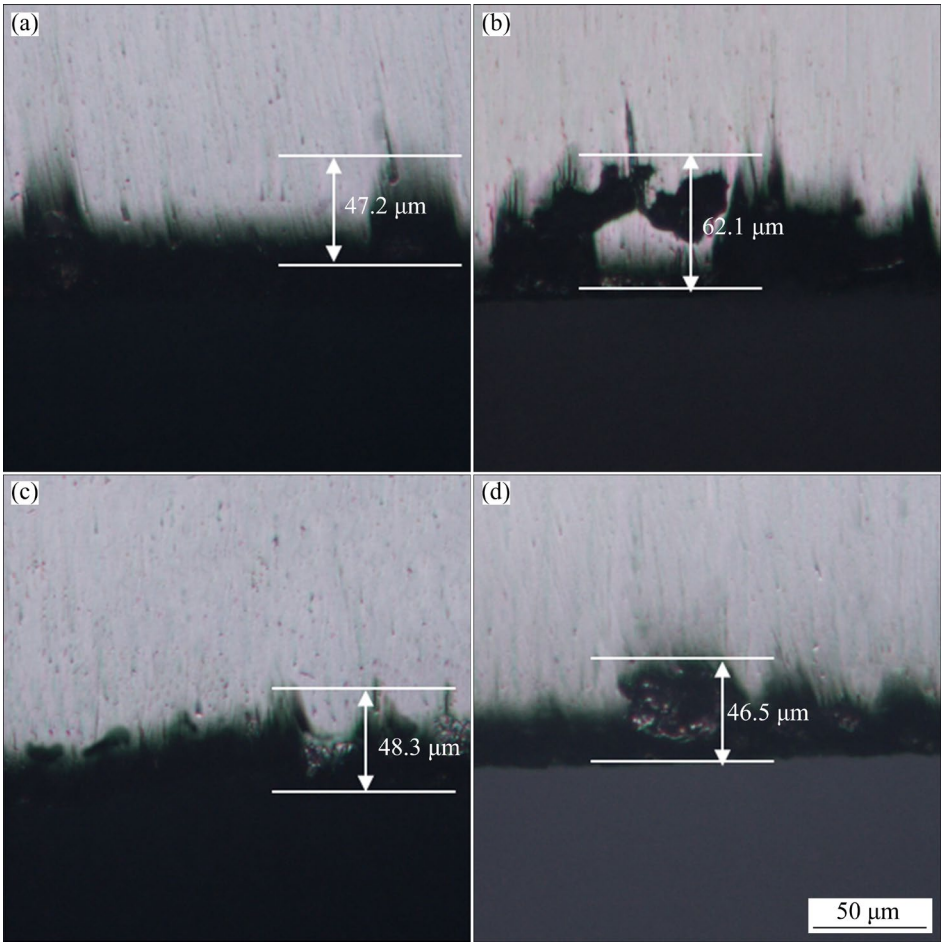

Fig. 6 Intergranular corrosion morphologies of 2195 Al−Li alloy after 24 h immersion: (a) UA; (b) PA; (c) DA; (d) RRA

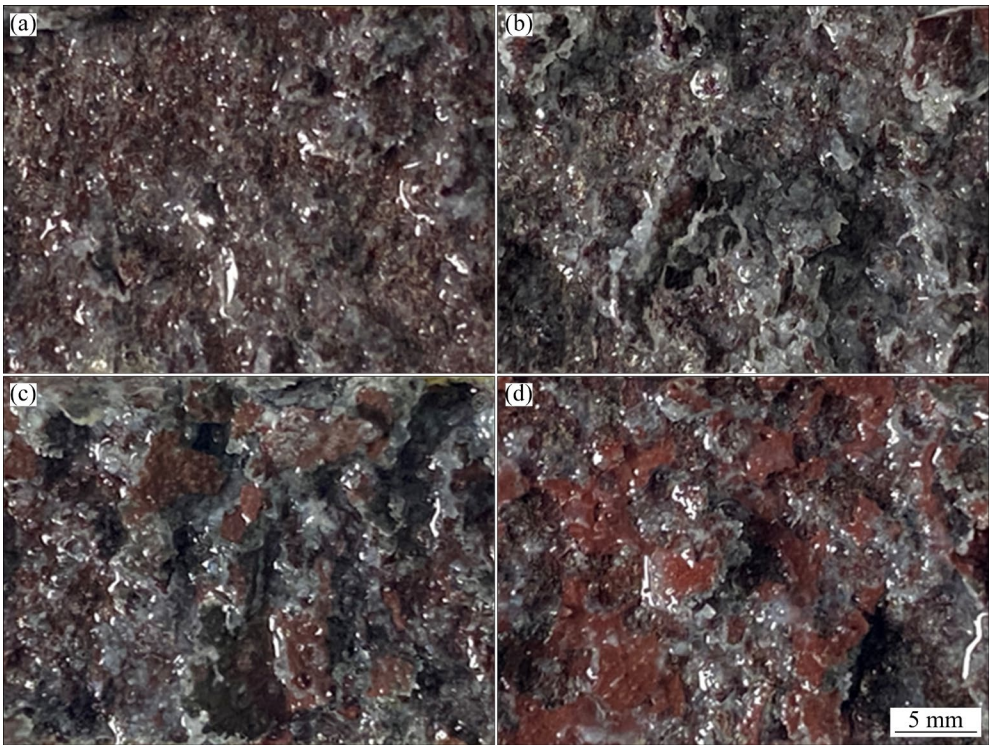

Fig. 7 Exfoliation corrosion morphologies of 2195 Al−Li alloy after 96 h immersion: (a) UA; (b) PA; (c) DA; (d) RRA

that corrode deep into the interior. The surface morphology of the alloy after DA treatment is similar to that of PA, with more severe surface peeling, thick reddish corrosion products, and serious delamination and peeling. The corrosion behavior of the surface in different regions of the alloy varies significantly under RRA. Some areas show no obvious peeling and delamination, indicating good resistance to peeling corrosion, but there are still a few areas with severe explosion and powdering and more pronounced corrosion pits of lower number and depth. By comparing the four corrosion morphologies, it can be observed that the corrosion trace becomes apparent after 96 h of corrosion, and the alloy exhibits good exfoliation corrosion resistance in UA and RRA states.

3.5 SCC behavior

3.5.1 Stress−strain curve

Figure 8 presents the stress−strain curves obtained from the slow strain rate test of the 2195 Al−Li alloy under different aging treatments in both air and 3.5% NaCl corrosive solution. The curves of the alloy in PA, DA, and RRA states as well as in air and 3.5% NaCl corrosive solution exhibit a similar trend. Initially, the stress increases rapidly with increasing strain, reaches a maximum value, and then gradually decreases until fracture occurs. However, the stress−strain curve of the UA state exhibits a distinct behavior, with a significantly lower rate of stress increase as strain increases, and rapid fracture after reaching a stable value.

In this test, the stress corrosion cracking sensitivity factor (I_{SSRT}) was used to quantitatively analyze the stress corrosion resistance of the alloy in different aging states, and the formula for the I_{SSRT} is as follows:

$$I_{SSRT}=1-\frac{\sigma_C(1+\delta_C)}{\sigma_A(1+\delta_A)} \quad (1)$$

where σ_C corresponds to tensile strength in 3.5% NaCl corrosive solution whereas σ_A corresponds to tensile strength in the air; δ_C and δ_A represent the elongation in 3.5% NaCl solution and air, respectively. The smaller the value, the smaller the difference between the alloy in the corrosion solution and the air, and the lower the sensitivity to the corrosion solution.

Table 2 indicates that the PA state exhibits the lowest elongation in both air and 3.5% NaCl solution,

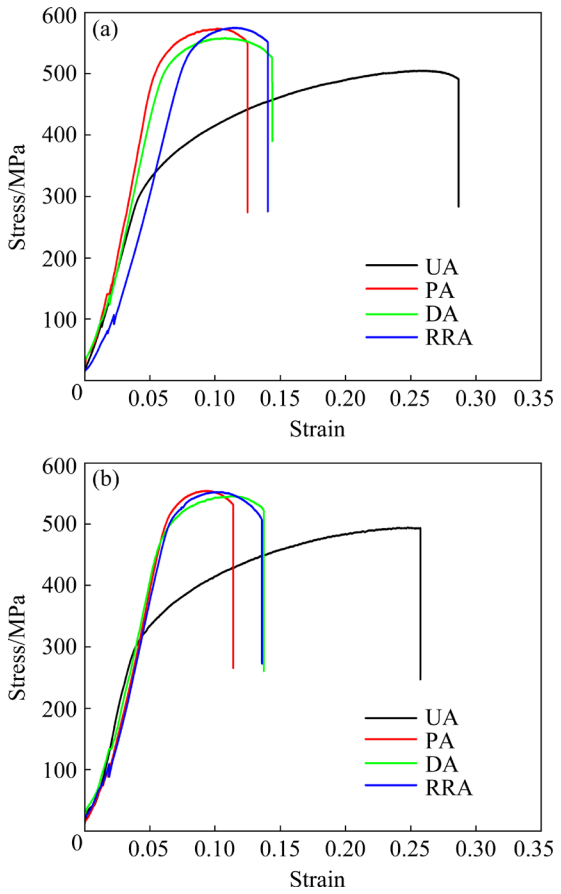

Fig. 8 Slow strain rate tensile curves of 2195 Al−Li alloy in different states: (a) In air; (b) In 3.5% NaCl solution

Table 2 Mechanical properties and I_{SSRT} of 2195 Al−Li alloy in different aging states in air and 3.5% NaCl solution

Aging treatment	Corrosive solution	Tensile strength/MPa	Elongation/%	I_{SSRT}/%
UA	Air	500	28.6	3.82
	3.5 wt.% NaCl	492	25.7	
PA	Air	572	12.5	6.00
	3.5 wt.% NaCl	543	11.4	
DA	Air	556	14.4	3.38
	3.5 wt.% NaCl	541	13.7	
RRA	Air	563	14.0	2.47
	3.5 wt.% NaCl	551	13.6	

but the highest tensile strength, reaching 572 MPa in air. In contrast, the UA state exhibits lower tensile strength but the highest elongation of 28.6%. The RRA state displays higher tensile strength compared to the DA state, in both air and

3.5% NaCl corrosive solution, but the elongation decreases, with a 0.4% reduction in the elongation of the samples in the corrosive solution. The I_{SSRT} calculations show that the PA state has the largest value of 6.00%, followed by the UA and DA states, whereas the RRA state has the smallest value of only 2.47%. These results demonstrate that the RRA treatment can significantly enhance the SCC resistance of alloy.

3.5.2 Stress corrosion fracture analysis

Figure 9 illustrates the fracture morphologies of the samples subjected to different aging regimes after SSRT experiments. The fracture morphologies in air and 3.5% NaCl corrosive solution are shown in Figs. 9(a_1−d_1) and (a_2−d_2), respectively. As seen from the figure, each fracture surface exhibits a number of dimples and transgranular fracture zones, as well as layered characteristics along the grain boundary.

Figure 9(a_1) illustrates that the surface of the fracture is dotted with numerous fine equiaxed dimples and holes, along with significant tearing edges, showing typical characteristics of ductile transgranular fracture [29]. In contrast, when the alloy fractures in the 3.5% NaCl corrosive solution, the number of dimples present at the fracture site is lesser, and their size becomes larger. Moreover, the number of tearing edges significantly reduces, resulting in relatively decreased elongation. Similar characteristics are evident in the PA state, whether in the 3.5% NaCl corrosive solution or in air. Specifically, the tensile fracture appears bright and smooth, with almost no dimples observable at the fracture. Additionally, the propagation of the crack and the delamination of the grain boundary are noticeable, revealing the features of quasi-cleavage fracture, which is a typical intergranular fracture. The pits at the grain boundary have been entirely corroded, indicating that the stress corrosion sensitivity of this sample is the worst. On the fracture surface of DA state samples fractured in air, a large number of cross-distributed tearing edges of significantly smaller size than the UA state exist, and a small number of fine dimples exist around the tearing edges, displaying the characteristics of transgranular ductile fracture. Additionally, some areas of grain boundary delamination are visible, which belong to dimple intergranular mixed fracture. When the alloy fails in the 3.5% NaCl corrosion solution, clear grain morphology and obvious propagation cracks can be observed, and the number of fine and deep dimples is also significantly reduced, which is related to the decrease of elongation. The fracture surfaces of the RRA state fractured in both air and 3.5% NaCl corrosive solution exhibit very few tearing edges and fine dimples. Instead, they display more grain boundary delamination, indicating that intergranular fracture is the main fracture mode after RRA treatment.

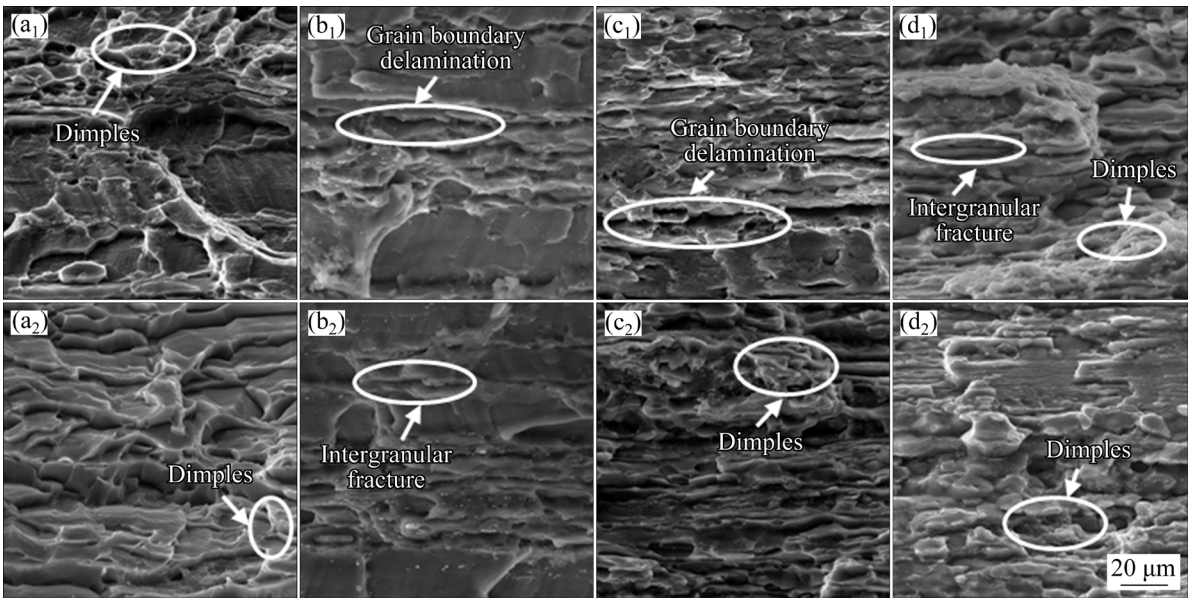

Fig. 9 Fracture surface morphologies of 2195 Al−Li alloy after SSRT test in air (a_1−d_1) and 3.5% NaCl corrosion solution (a_2−d_2): (a_1, a_2) UA; (b_1, b_2) PA; (c_1, c_2) DA; (d_1, d_2) RRA

4 Discussion

4.1 Microstructure evolution during aging

Current research shows that the aging precipitation sequence of Al−Cu−Li alloy is: SSS → GP zone + δ' → θ'' + θ' + δ'→ δ' + T_1 → T_1, when Cu/Li=2−5. In the natural aging state, the main precipitation strengthening phases are the GP zone and δ' phase, while during artificial aging, the δ' phase gradually transforms into δ', T_1, and θ' phases [30,31]. When the aging temperature increased to 155 °C, the θ'' and δ' phases precipitated at low temperature gradually dissolved, and the T_1 phase became the main precipitated phase [32].

In this experiment, the type and morphology of precipitates in the 2195 Al−Li alloy differ significantly in different aging states. Specifically, in the UA state, δ' and θ' precipitates form early due to high coherency and low interfacial energy. In contrast, the T_1 phase, which is semi-coherent with the matrix and has higher interfacial energy, tends to nucleate at sites of dislocations, grain boundaries, subgrain boundaries, stacking faults, and vacancy clusters, leading to late-stage precipitation. Upon reaching the PA state, a large number of T_1 phases with larger sizes precipitate within the grains. This may be due to the release of Cu atoms via diffusion dissolution from numerous semi-coherent transition θ' phases.

The microstructure of 2195 Al−Li alloy treated by two-stage aging is significantly different from that of single-stage aging, which is due to the formation of high density diffusely distributed GP zone in the alloy during the low-temperature aging stage at 120 °C for 8 h. Subsequently, the high-temperature aging treatment at 170 °C for 18 h serves two purposes: promoting the transformation of the GP zone to the transition phase and driving the phase transformation to the stable T_1 phase due to interfacial energy. Additionally, some of the second phase that has already precipitated at the grain boundary may grow rapidly.

After RRA treatment, the sample is characterized by the intracrystalline diffusely precipitated T_1 phases as well as intermittently distributed T_1 phases at grain boundaries, which may be attributed to three different aging steps. Firstly, the alloy undergoes pre-aging at the PA temperature after solution quenching, resulting in a high density of fine dispersion strengthening phases within the grain and a continuous second phases precipitated at the grain boundary. Then, short-term retrogression treatment at a higher temperature (220 °C, 40 min) causes unstable precipitates smaller than the critical size in the grain to dissolve back into the matrix. While stable T_1 phases with larger sizes continue to grow, and Cu-rich and T_1 phases start to aggregate and grow at the grain boundary, losing continuity with each other and showing discontinuous distribution. Finally, during T6 treatment, fine and high-density dispersion strengthening phases are precipitated within the grain again. The precipitated phases at the grain boundary undergo further coarsening and become discontinuous, and the bandwidth of PFZ increases.

4.2 Relationship between aging regime and corrosion performance

The above studies on IGC and EXCO show that 2195 Al−Li alloy is sensitive to corrosion, and it has the same resistance to IGC and EXCO (RRA > UA > DA > PA). Based on the results of corrosion tests and corresponding microstructural characteristics of the above experimental samples, the effect of different aging treatments on the corrosion resistance of 2195 Al−Li alloy is discussed. It is generally believed that EXCO is a special form of IGC, therefore, the mechanism of aging on IGC and EXCO will be discussed together.

The relationship among the corrosion potential of the PFZ, T_1 and θ' phases can be expressed as θ' > PFZ > T_1 [33−35]. Therefore, it can be assumed that T_1 phase dissolves as the anode and the aluminum matrix (equivalent to PFZ) is protected as the cathode during the corrosion process. When the alloy is in the UA state, the grain contains mainly small T_1 and θ' precipitates, hindering the continuity of corrosion channels. As a result, the corrosion susceptibility of the alloy is relatively low at the beginning of aging. As the aging time is extended to the PA state, mass larger T_1 phases are formed in the grain, and the precipitates at the grain boundary are continuously precipitated and coarsened, promoting the formation of PFZ. Meanwhile, it causes a potential difference among the matrix, precipitates, and PFZ, which in turn

promotes the formation of corrosion cracks and worsens the occurrence of IGC. In the DA state, small-sized δ', θ' and T_1 phases are uniformly distributed in the matrix, reducing the enrichment of each element and the potential difference between the matrix and precipitates. Additionally, the intermittent distribution of partly precipitates at the grain boundary can hinder the expansion of corrosion cracks, contributing to the alloy's corrosion resistance. However, it is also noted that the narrower width of the PFZ band leads to a narrower path for anodic dissolution, increasing the rate of corrosion.

The precipitates in the RRA state are still dominated by the T_1 phase, but the precipitates have grown and coarsened significantly. When the grain boundary precipitates grow, the spacing between them becomes wider and discontinuous, which interrupts the corrosion channel at the grain boundary and improves the intergranular corrosion resistance of the alloy. After RRA treatment, the sample obtained a wider PFZ than the other three aging states, with a value of 125 nm, balancing the potential between grain and grain boundary and weakening the tendency of anodic dissolution. This reduces the corrosion susceptibility of the alloy, making it more resistant to IGC and EXCO. In conclusion, the coarsening and discontinuous distribution of grain boundary precipitates as well as the broadening of PFZ are conducive to reducing the corrosion sensitivity of the alloy.

4.3 Stress corrosion behavior and mechanism

Anodic dissolution and hydrogen-induced cracking hypothesis are currently the two theories most commonly used to describe the stress corrosion cracking mechanism of Al−Li alloy. It is shown that the stress corrosion susceptibility of the alloy is mainly affected by the size of the matrix precipitation phase, the size and distribution of the grain boundary precipitation phase, the width of the PFZ, the solute concentration gradient, and so on [36,37]. Based on the obtained experimental results, a schematic diagram of the stress corrosion mechanism of the 2195 Al−Li alloy under different aging regimes was established as shown in Fig. 10. The passive film on the alloy surface contains both matrix and precipitated phase, and when it is placed in the corrosive solution, it is subjected to both tensile stress and local electrochemical reaction, and pitting is prone to occur around the T_1, θ' phase and grain boundaries, causing dissolution of the passive film and the formation of initial microcracks. The chloride ions in the corrosive solution continue to attack the defect, and the exposed matrix and precipitated phases continuously undergo electrochemical reactions, producing continuous pitting pits distributed along the grain boundary. Eventually, his leads to the formation of crack growth channels and crack expansion along the grain boundary until fracture failure occurs [38].

The precipitated phase in the grain is relatively few in the UA state, and the intergranular bonding is tight, resulting in a relatively large deformation required to produce cracking, and the slip can cross the grain boundary from one grain to another. Under the action of tensile stress, the stress concentration at the crack tip causes local plastic deformation and accelerates the dissolution of the phase at the grain boundary, which results in crack initiation and propagation. In the PA state, the precipitates at the grain boundary are coarser and continuous, dislocations are not easy to slip across the grain boundary, and plastic deformation is limited within the PFZ, so cracks mainly extend along the grain boundary. Meanwhile, the rise in corrosion driving force is caused by the increase in

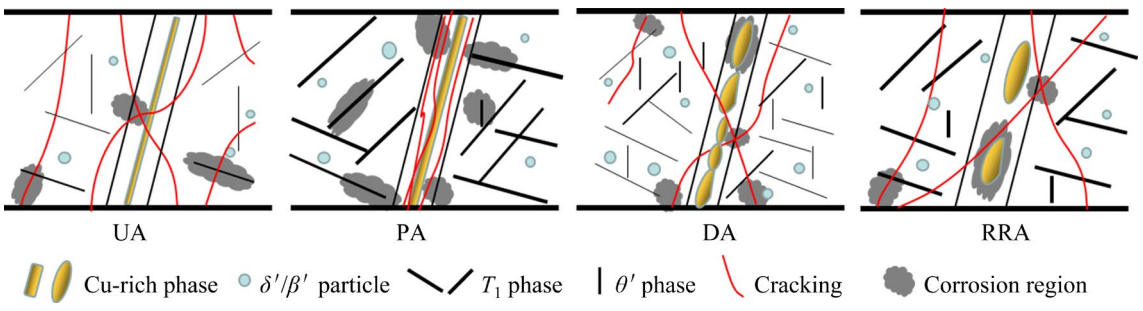

Fig. 10 Schematic diagram of stress corrosion mechanism of 2195 Al−Li alloy in different aging states

the potential difference between the precipitated phase and PFZ, which in turn contributes to a severe degree of stress corrosion fracture. The corrosion fracture due to anodic dissolution usually shows the characteristics of intergranular fracture, while the stress corrosion fracture in the PA state has a smooth surface without obvious dimples, and the corrosion cracks extend along the grain boundaries, showing the typical intergranular fracture characteristics, therefore, it can be indicated that the main mechanism of fracture in PA state is anodic dissolution.

When the alloy is treated with DA and RRA, the isolated distribution of the precipitated phases at the grain boundary can reduce the stacking of dislocations at the grain boundary [39], allowing corrosion cracks to extend across the grain boundary, thus contributing to higher fracture elongation. In addition, the discontinuously distributed grain boundary precipitates can reduce the number of electrode pairs while also absorbing some hydrogen atoms so that they cannot form hydrogen atom bubbles, thus improving the stress corrosion resistance of the alloy. Compared with the DA state, the RRA state has wider PFZ, so it has better resistance to stress corrosion. The fracture morphology also shows that, in addition to the corrosion cracks that extend continuously at the grain boundaries on the fracture surface, there are also a small number of tiny dimples around the tearing edges. This illustrates that the intergranular-transgranular mixed fracture mainly occurs, indicating a mixed hydrogen embrittlement-anodic dissolution mechanism for the failure. RRA precipitates mainly consist of larger T_1 phases, while DA precipitates mainly consist of smaller and denser T_1 and θ' phases. However, the RRA state shows better resistance to stress corrosion, suggesting that dissolution of precipitated phase at the grain boundary may be the main cause of stress corrosion cracking of the alloy.

5 Conclusions

(1) The precipitates inside the grain mainly consist of δ'/β', θ' and T_1 phases under early aging condition, while in the PA state, a large amount of T_1 phases precipitate within the grains and at the grain boundaries. In the DA state, a quantity of small-sized θ' and T_1 phases precipitate inside the grain, and part of the precipitates intermittently distributed along the grain boundary. After RRA treatment, T_1 phases with a larger size, wider spacing and discontinuous distribution are precipitated at the grain boundary, and the width of PFZ also increases to 125 nm.

(2) The results of IGC and EXCO tests reveal that the corrosion resistance of 2195 Al−Li alloy is RRA > UA > DA > PA. The continuous precipitates at the grain boundary are primarily responsible for the low corrosion resistance of PA and UA states. The RRA state shows the best IGC and EXCO resistance owing to the discontinuous distribution of coarse T_1 phases at the grain boundary and the widest PFZ band, thereby interrupting the grain boundary corrosion channels.

(3) The SCC resistance of 2195 Al−Li alloy is as follows: RRA > DA > UA > PA. The PA state exhibits the inferior SCC resistance (I_{SSRT} is 6.00%), mainly due to the continuously distributed coarse precipitates at the grain boundary, causing incipient corrosion cracks to propagate along the grain boundary. The RRA-treated sample displays the best SCC resistance (I_{SSRT} is 2.47%), resulting from a large amount of T_1 phases precipitated inside grain and at the grain boundary, which maintains the equilibrium of the corrosion potential between the grain and the grain boundary, and allows the corrosion crack to propagate across the grain boundary under tensile stress.

CRediT authorship contribution statement

Hui LI: Conceptualization, Data curation, Investigation, Methodology, Validation, Writing – Original draft, Writing – Review & editing; **Zhi-wen WANG:** Investigation; **Rong FU:** Investigation; **Yuan-chun HUANG:** Supervision, Project administration, Writing – Review & editing.

Declaration of competing interest

The authors declare that they have no known competing financial interests or personal relationships that could have appeared to influence the work reported in this paper.

Acknowledgments

This work is financially supported by the National Natural Science Foundation of China (No. U1837207).

References

[1] WILLIAMS J C, STARKE E A Jr. Progress in structural materials for aerospace systems [J]. Acta Materialia, 2003, 51(19): 5775−5799.

[2] HE Guo-ai, LI Kai, YANG Yong, LIU Yu, WU Wen-kai, HUANG Cheng. Effect of heat treatment on the microstructure and mechanical properties of cryogenic rolling 2195 Al−Cu−Li alloy [J]. Materials Science and Engineering: A, 2021, 822: 141682.

[3] XIE Bing-xin, HUANG Liang, XU Jia-hui, SU Hong-liang, ZHANG Hui-ping, XU Yi-ke, LI Jian-jun, WANG Yu. Effect of the aging process and pre-deformation on the precipitated phase and mechanical properties of 2195 Al−Li alloy [J]. Materials Science and Engineering: A, 2022, 832: 142394.

[4] GHOSH R, VENUGOPAL A, NARAYANAN P R, SHARMA S C, VENKITAKRISHNAN P V. Environmentally assisted cracking resistance of Al−Cu−Li alloy AA2195 using slow strain rate test in 3.5% NaCl solution [J]. Transactions of Nonferrous Metals Society of China, 2017, 27(2): 241−249.

[5] WANG Xue-hui, WANG Ji-hui, YUE Xin, GAO Yun. Effect of aging treatment on the exfoliation corrosion and stress corrosion cracking behaviors of 2195 Al−Li alloy [J]. Materials & Design, 2015, 67: 596−605.

[6] PROTON V, ALEXIS J, ANDRIEU E, DELFOSSE J, DESCHAMPS A, de GEUSER F, LAFONT M C, BLANC C. The influence of artificial ageing on the corrosion behaviour of a 2050 aluminium–copper–lithium alloy [J]. Corrosion Science, 2014, 80: 494−502.

[7] GUÉRIN M, ALEXIS J, ANDRIEU E, BLANC C, ODEMER G. Corrosion-fatigue lifetime of Aluminium–Copper–Lithium alloy 2050 in chloride solution [J]. Materials & Design, 2015, 87: 681−692.

[8] XU Xiao-jing, HAO Min, CHEN Jun-zhou, HE Wei-wei, LI Guo-ai, LI Ke-xue, JIAO C, ZHONG Xiang-li, MOORE K L, BURNETT T L, ZHOU Xiao-rong. Role of constituent intermetallic phases and precipitates in initiation and propagation of intergranular corrosion of an Al−Li−Cu−Mg alloy [J]. Corrosion Science, 2022, 201: 110294.

[9] KNIGHT S P, BIRBILIS N, MUDDLE B C, TRUEMAN A R, LYNCH S P. Correlations between intergranular stress corrosion cracking, grain-boundary microchemistry, and grain-boundary electrochemistry for Al−Zn−Mg−Cu alloys [J]. Corrosion Science, 2010, 52(12): 4073−4080.

[10] WEN Sheng-ping, GAO Kun-yuan, LI Yan, HUANG Hui, NIE Zuo-ren. Synergetic effect of Er and Zr on the precipitation hardening of Al−Er−Zr alloy [J]. Scripta Materialia, 2011, 65(7): 592−595.

[11] MA Yan-long, ZHOU Xiao-rong, MENG Xiao-min, HUANG Wei-jiu, LIAO Yi, CHEN Xiao-li, YI Ya-yan, ZHANG Xin-xin, THOMPSON G E. Influence of thermomechanical treatments on localized corrosion susceptibility and propagation mechanism of AA2099 Al−Li alloy [J]. Transactions of Nonferrous Metals Society of China, 2016, 26(6): 1472−1481.

[12] HOLROYD N J H, SCAMANS G M, NEWMAN R C, VASUDEVAN A K. Corrosion and stress corrosion of aluminum–lithium alloys [M]//ESWARA PRASAD N, GOKHALE A A, WANHILL R J H. Aluminum-lithium Alloys. Boston; Butterworth-Heinemann. 2014: 457−500.

[13] LIN Yi, LU Chan-ge, WEI Cheng-yang, ZHENG Zi-qiao. Effect of aging treatment on microstructures, tensile properties and intergranular corrosion behavior of Al−Cu−Li alloy [J]. Materials Characterization, 2018, 141: 163−168.

[14] ROMIOS M, TIRASCHI R, OGREN J R, ES-SAID O S, PARRISH C, BABEL H W. Design of multistep aging treatments of 2099 (C458) Al−Li alloy [J]. Journal of Materials Engineering and Performance, 2005, 14(5): 641−646.

[15] WANG Tao, YANG Lun, TANG Zhao-feng, LIU Chao, MA Yun-zhu, WU Lei, YAN Huan-yuan, YU Zhao-ji, LIU Wen-sheng. Effect of aging treatment on microstructure, mechanical and corrosion properties of 7055 aluminum alloy prepared using powder by-product [J]. Materials Science and Engineering: A, 2021, 822: 141606.

[16] WANG Yi-chang, CAO Ling-fei, WU Xiao-dong, TONG Xin, LIAO Bin, HUANG Guang-jie, WANG Zheng-an. Effect of retrogression treatments on microstructure, hardness and corrosion behaviors of aluminum alloy 7085 [J]. Journal of Alloys and Compounds, 2020, 814: 152264.

[17] YUAN Ding-ling, CHEN Kang-hua, CHEN Song-yi, ZHOU Liang, CHANG Jiang-yu, HUANG Lan-ping, YI You-ping. Enhancing stress corrosion cracking resistance of low Cu-containing Al−Zn−Mg−Cu alloys by slow quench rate [J]. Materials & Design, 2019, 164: 107558.

[18] LI Jin-feng, BIRBILIS N, LI Chao-xing, JIA Zhi-qiang, CAI Biao, ZHENG Zi-qiao. Influence of retrogression temperature and time on the mechanical properties and exfoliation corrosion behavior of aluminium alloy AA7150 [J]. Materials Characterization, 2009, 60(11): 1334−1341.

[19] KAIRY S K, TURK S, BIRBILIS N, SHEKHTER A. The role of microstructure and microchemistry on intergranular corrosion of aluminium alloy AA7085-T7452 [J]. Corrosion Science, 2018, 143: 414−427.

[20] GHOSH K S, SAS K, CHATTERJEE U K. Studies of microstructural changes upon retrogression and reaging (RRA) treatment to 8090 Al−Li−Cu−Mg−Zr alloy [J]. Materials Science and Technology, 2004, 20: 825−834.

[21] GHOSH K S, CHATTERJEE U. Studies of retrogression and reaging behavior in a 1441 Al−Li−Cu−Mg−Zr alloy [J]. Metallurgical and Materials Transactions A, 2005, 36: 3477−3487.

[22] WARD N, TRAN A, ABAD A, LEE E W, HAHN M, FORDAN E, ES-SAID O. The effects of retrogression and reaging on aluminum alloy 2195 [J]. Journal of Materials Engineering and Performance, 2011, 20: 1003−1014.

[23] LI Hong-ying, TANG Yi, ZENG Zai-de, ZHENG Zi-qiao, ZHENG Feng. Effect of ageing time on strength and microstructures of an Al−Cu−Li−Zn−Mg−Mn−Zr alloy [J]. Materials Science and Engineering: A, 2008, 498(1): 314−320.

[24] HOWE J M, LEE J, VASUDÉVAN A K. Structure and deformation behavior of T1 precipitate plates in an Al−2Li−1Cu alloy [J]. Metallurgical and Materials Transactions A, 1988, 19(12): 2911−2920.

[25] GUMBMANN E, de GEUSER F, SIGLI C, DESCHAMPS A. Influence of Mg, Ag and Zn minor solute additions on the precipitation kinetics and strengthening of an Al−Cu−Li alloy [J]. Acta Materialia, 2017, 133: 172−185.
[26] DESCHAMPS A, GARCIA M, CHEVY J, DAVO B, de GEUSER F. Influence of Mg and Li content on the microstructure evolution of Al−Cu−Li alloys during long-term ageing [J]. Acta Materialia, 2017, 122: 32−46.
[27] NING Jian, LI Qun, ZOU Zong-yuan, LIU Tian-wei, CHEN Lei. Hot tensile deformation behavior and microstructural evolution of 2195 Al−Li alloy [J]. Vacuum, 2021, 188: 110176.
[28] HUANG Jia-ying, MING Wen-quan, WU Cui-lan, Effect of microstructure on corrosion behaviour of Al−Cu−Li alloys [J]. Materials Characterization, 2022, 194: 112416.
[29] ZHOU Chang, ZHAN Li-hua, LI He, ZHAO Xing, CHEN Fei, HUANG Ming-hui. Creep ageing behaviour assisted by electropulsing under different stresses for Al−Cu−Li alloy [J]. Transactions of Nonferrous Metals Society of China, 2021, 31(7): 1916−1929.
[30] KUMAR K S, HEUBAUM F H. The effect of Li content on the natural aging response of Al−Cu−Li−Mg−Ag−Zr alloys [J]. Acta Materialia, 1997, 45(6): 2317−2327.
[31] ZHANG Sai-fei, ZENG Wei-dong, YANG Wen-hua, SHI Chun-ling, WANG Hao-jun. Ageing response of a Al−Cu−Li 2198 alloy [J]. Materials & Design, 2014, 63: 368−374.
[32] ARAULLO-PETERS V, GAULT B, GEUSER F D, de SCHAMPS A, CAIRNEY J M. Microstructural evolution during ageing of Al−Cu−Li−x alloys [J]. Acta Materialia, 2014, 66: 199−208.
[33] de SOUZA CARVALHO, MACHADO C, DONATUS U, MILAGRE M X, ARAUJO J V, de VIVEIROS B V G, KLUMPP R E, PEREIRA V F, COSTA I. How microstructure affects localized corrosion resistance of stir zone of the AA2198-T8 alloy after friction stir welding [J]. Materials Characterization, 2021, 174: 111025.
[34] LI Jin-feng, ZHENG Zi-qiao, JIANG Na, TAN Cheng-yu. Localized corrosion mechanism of 2×××-series Al alloy containing $S(Al_2CuMg)$ and $\theta'(Al_2Cu)$ precipitates in 4.0% NaCl solution at pH 6.1 [J]. Materials Chemistry and Physics, 2005, 91(2): 325−329.
[35] LI Jin-feng, LI Chao-xing, PENG Zhuo-wei, CHEN Wen-jing, ZHENG Zi-qiao. Corrosion mechanism associated with T1 and T2 precipitates of Al−Cu−Li alloys in NaCl solution [J]. Journal of Alloys and Compounds, 2008, 460(1): 688−693.
[36] LI Hong-ying, KANG Wei, LU Xiao-chao. Effect of age-forming on microstructure, mechanical and corrosion properties of a novel Al−Li alloy [J]. Journal of Alloys and Compounds, 2015, 640: 210−218.
[37] KRISHNAN M A, RAJA V S. Development of high strength AA 7010 aluminum alloy resistant to environmentally assisted cracking [J]. Corrosion Science, 2016, 109: 94−100.
[38] MCNAUGHTAN D, WORSFOLD M, ROBINSON M J. Corrosion product force measurements in the study of exfoliation and stress corrosion cracking in high strength aluminium alloys [J]. Corrosion Science, 2003, 45(10): 2377−2389.
[39] BALDUCCI E, CESCHINI L, MESSIERI S, WENNER S, HOLMESTAD R. Thermal stability of the lightweight 2099 Al−Cu−Li alloy: Tensile tests and microstructural investigations after overaging [J]. Materials & Design, 2017, 119: 54−64.

时效处理对 2195 Al−Li 合金挤压型材腐蚀行为的影响

李 辉[1,2]，王志文[3]，付 绒[1,2]，黄元春[1,2,3]

1. 中南大学 机电工程学院，长沙 410083；
2. 中南大学 高性能复杂制造国家重点实验室，长沙 410083；
3. 中南大学 轻合金研究院，长沙 410083

摘 要：对 2195 铝锂合金分别进行欠时效(UA)、峰时效(PA)、双级时效(DA)和回归再时效(RRA)处理，观察并讨论其显微组织、晶间腐蚀(IGC)、剥落腐蚀(EXCO)和应力腐蚀开裂(SCC)行为。结果表明，合金经不同时效处理后，其 IGC 和 EXCO 耐蚀性顺序为：RRA>UA>DA>PA。PA 和 UA 态的低耐蚀性主要是 T_1 相在晶界处连续析出形成连续的腐蚀通道引起的，而粗大不连续析出的 T_1 相以及较宽的无析出带导致的腐蚀通道中断是 RRA 态具有最佳耐蚀性的原因。RRA 态合金表现出最好的抗应力腐蚀性能，抗应力腐蚀顺序为：RRA>DA>UA>PA。晶间 T_1 相的不连续析出促进了腐蚀裂纹穿过晶界进行扩展，从而提高了 2195 铝锂合金的抗应力腐蚀性能。

关键词：时效；显微组织演变；腐蚀行为；腐蚀机理

(Edited by Xiang-qun LI)